



# Effect of Deformation Sequence and Coiling Conditions on Precipitation Strengthening in High Ti–Nb–Microalloyed Steels

L.G. SESMA, B. LOPEZ, and B. PEREDA

In this work, multipass torsion tests followed by coiling simulations under different conditions have been performed with a reference Nb (0.03 pct) and a high Ti (0.1 pct)–Nb–microalloyed (0.03 pct) steel. In the case of the high Ti steel, estimated yield strengths close to or over 700 MPa were obtained for some of the conditions researched. However, a very significant effect of previous austenite grain size and strain accumulation on precipitation strengthening has also been observed. As a result, depending on deformation sequence and final cooling conditions, the coiling simulation temperatures that lead to the highest mechanical strength varied from 600 °C to 500 °C. The effect of increasing strain accumulation was mainly related to higher phase transformation temperatures, which led to a lower driving force for precipitation and higher microalloying element diffusivity, resulting in the formation of less and coarser precipitates.

<https://doi.org/10.1007/s11661-022-06670-w>  
© The Author(s) 2022

## I. INTRODUCTION

IN the case of low-carbon steels, when high-strength and low-temperature toughness properties are required, the addition of microalloying elements, such as Nb, V, Mo, or Ti is a common practice. Niobium is most frequently used due to the retarding effect that it exerts on the softening processes during hot deformation by solute drag and/or strain-induced precipitation, which produces refined room-temperature microstructures with enhanced grain size strengthening. Nb can also provide some hardenability, thus, favoring the appearance of non-equilibrium phases.<sup>[1]</sup> Titanium, in conventional addition levels (< 0.03 pct), can contribute to microstructural refinement by suppressing austenite grain growth during hot deformation due to the pinning effect exerted by Ti(C,N) precipitates.<sup>[2]</sup> However, in recent years, special attention has been paid to the large precipitation-strengthening potential of high Ti additions ( $\cong$  0.05 pct) in low-carbon steels, due to the development of fine precipitate dispersion during or after  $\gamma \rightarrow \alpha$  phase transformation.<sup>[3,4]</sup> With this microalloying concept, very high strength combined with good ductility and great uniform elongation can be

achieved.<sup>[5,6]</sup> Usually, high Ti additions are applied in combination with other microalloying elements, such as Nb,<sup>[7,8]</sup> Mo,<sup>[9]</sup> or V.<sup>[10]</sup> The Ti–Mo combination has been the most researched microalloying concept,<sup>[11]</sup> since it is reported that Mo leads to a refinement of the precipitates formed during phase transformation and, as a result, to higher precipitation hardening potential. This effect has been attributed to precipitate/matrix interphase segregation of Mo,<sup>[12]</sup> higher dislocation density owing to the hardenability exerted by Mo,<sup>[12]</sup> or to a reduction in misfit strain at the precipitate/ferrite interface.<sup>[13]</sup> However, there is still uncertainty regarding the cause of this precipitation refinement effect.

Some works have also considered the potential of other microalloying combinations, showing that significant precipitation strengthening can also be achieved with Ti alone,<sup>[14]</sup> or in combination with Nb<sup>[15]</sup> or V.<sup>[10]</sup> However, major dependence of precipitation strengthening on final cooling conditions has also been observed. In these steels, mechanical property variability at similar processing conditions or within the same rolled product at different positions is one of the main problems concerning their applicability.<sup>[16]</sup> One of the reasons for this effect is the variability in size and volume fraction of the precipitates formed during phase transformation, which greatly depend on final coiling temperature or cooling rate.<sup>[15,17,18]</sup> As a result, in many works, the dependence of mechanical strength on final cooling conditions has been researched,<sup>[8,15,19,20]</sup> although this is not the only factor that can affect precipitation strengthening. For instance, it has been observed that the addition of elements that increase hardenability, such as

L.G. SESMA, B. LOPEZ, and B. PEREDA are with the Materials and Manufacturing Division, Ceit-Basque Research and Technology Alliance (BRTA), Manuel Lardizabal 15, 20018 Donostia/San Sebastián Spain and also with the Universidad de Navarra, Teenu, Manuel Lardizabal 13, 20018 Donostia/San Sebastián Spain. Contact e-mail: bpereda@ceit.es.

Manuscript submitted December 22, 2021; accepted March 17, 2022.

Article published online April 11, 2022

Mn or Cr,<sup>[21,22]</sup> may modify phase transformation conditions and, as a result, the volume fraction and size of the precipitates formed during phase transformation. In the case of Ti–Nb steels, the effect of Nb also needs to be considered. The conventional role of Nb in low-carbon-microalloyed steels is to retard austenite recrystallization during austenite hot deformation, leading to refined final room-temperature microstructures.<sup>[23–26]</sup> However, this can also influence transformation conditions, and therefore, affect optimum cooling conditions. To analyze this, in this work, multipass torsion tests that result in different austenite microstructures, followed by coiling simulations at different temperatures and final cooling rates, have been performed with a high Ti–Nb-microalloyed steel and a reference Nb-microalloyed steel.

## II. EXPERIMENTAL PROCEDURE

The composition of the steels subject to research is shown in Table I (wt pct). A reference 0.03 pct Nb low-carbon-microalloyed steel (Ti0Nb3), and a steel with a high Ti addition of 0.1 pct and similar Nb content (Ti10Nb3) were analyzed.

Torsion tests were performed, followed by thermal cycles that simulate different coiling conditions. The torsion specimens consisted of a gage-type geometry of 16.5 mm in length and 7.5 mm in diameter. Two multipass deformation schedules were applied: sequence A and B. The thermomechanical cycle applied in both cases is schematically represented in Figure 1, and the specific deformation and final cooling parameters are summarized in Table II and Table III, respectively. As shown in the figure, in all cases, the specimens were first reheated at 1250 °C for 20 minutes. Next, three roughing deformation passes were applied at temperatures between 1200 °C and 1100 °C, followed by 4 finishing passes from 1030 °C to 900 °C. As indicated in Table II, the deformation temperature ( $T$ ), interpass time ( $t_{ip}$ ), and strain rate ( $\dot{\epsilon}$ ) per pass were the same for both cycles. In terms of strain ( $\epsilon_{pass}$ ), this was representative of that applied for hot rolling a slab of 40 to 4 mm final thickness. However, a different strain partition per pass was considered in the sequences: in sequence A, the strain applied during the finishing stage was higher than in cycle B, and, in addition, during finishing, the strain increases from pass to pass, while the opposite occurs in the case of sequence B. The aim was to obtain austenite microstructures with different degrees of strain accumulation prior to  $\gamma \rightarrow \alpha$  phase transformation.

After finishing, the specimens were fast cooled (13 °C/s) to coiling simulation start temperatures from 500 °C to 650 °C. The coiling period was simulated by final slow cooling at 0.03 °C/s or 0.01 °C/s to 200 °C followed by air cooling. These cooling rates may be considered representative of two different positions of a heavy coil (“strip center-mid-width” and “strip

edge”).<sup>[15]</sup> Interrupted tests were also performed by quenching at 850 °C to analyze the austenite microstructures present before final cooling simulation.

Metallographic analysis of the torsion specimens was conducted at the sub-surface section,<sup>[27]</sup> corresponding to 0.9 of the outer radius of the torsion specimen, as shown schematically in Figure 2(d). All the specimens were analyzed using optical microscopy. Bechet–Beaujard etching<sup>[28]</sup> was used to reveal the previous austenite grain boundaries in the quenched samples. 2 Pct Nital was used in most cases in the transformed samples, although, in some cases, Bechet–Beaujard etching provided better results revealing the microstructure, and thus, this reagent was applied. Electron backscatter diffraction (EBSD) scans were also collected in a field emission gun scanning electron microscopy (FEG-SEM) equipment, using a step size of 0.5  $\mu\text{m}$  and analysis areas of 450  $\times$  450  $\mu\text{m}^2$ . Standard cleanup grain dilation method was applied on the scans.<sup>[29]</sup> The EBSD grain sizes (equivalent circular diameter) were calculated according to the following expressions:

$$A = \text{npixels}(\text{stepsize})^2, \quad [1]$$

$$D = 2 \times \sqrt{\frac{A}{\pi}}. \quad [2]$$

A minimum grain size of 3 pixels is considered, which according to above equations corresponds to an equivalent diameter of 0.98  $\mu\text{m}$ .

Transmission electron microscopy (TEM) analysis was also carried out on selected samples to characterize the precipitation state in a JEM-2100 microscope operated at 200 kV. Both carbon extraction replicas and thin foils were analyzed, the latter prepared by the lift-out technique using a Quanta 3D FEG-focused ion beam-milling instrument (FIB). In addition to using diffraction contrast (dark field, DF), the precipitates were also imaged using the energy-filtered TEM (EFTEM) technique and jump-ratio method in the thin foils, which enables compositional maps to be obtained, in which the areas containing the element selected for analysis are contrasted, usually in white.<sup>[30]</sup> Overlapping Nb–N<sub>2,3</sub> and Ti–M<sub>2,3</sub> edges were employed to detect the precipitates, using conditions similar to those proposed in reference,<sup>[31]</sup> and the EFTEM technique was also used to compute thickness maps to measure the amount of particles per unit volume in the thin foils. Lastly, precipitate size measurements were performed in some samples in terms of the mean equivalent diameter (MED) parameter. The area corresponding to each precipitate is calculated using DigitalMicrograph™ software and then, for each precipitate, an equivalent diameter, which is the diameter of the circle with equal area is calculated. The average of all the diameters is the mean equivalent diameter.

**Table I. Chemical Composition of the Steels Investigated (Wt Pct)**

Steel	C	Mn	Nb	Ti	P	S	Al	Si	Cr	Ni	N
Ti0Nb3	0.059	1.79	0.033	0.003	0.020	0.003	0.036	0.026	0.013	0.005	0.0036
Ti10Nb3	0.059	1.80	0.034	0.091	0.021	0.003	0.036	0.016	0.017	0.006	0.0054

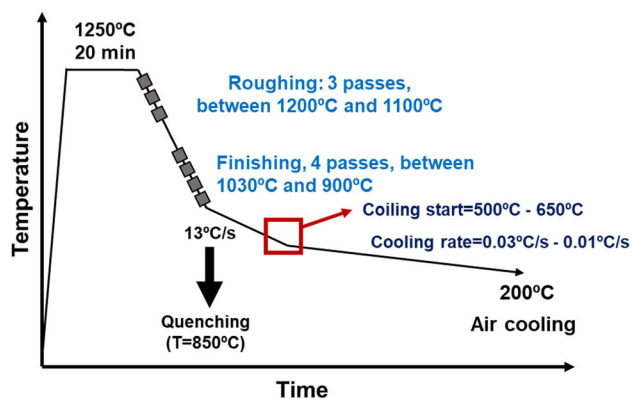


Fig. 1—Scheme of the thermomechanical cycles applied in this work.

**Table II. Deformation Conditions Employed in the Simulations**

$T$ (°C)	$\dot{\epsilon}$ (s <sup>-1</sup> )	$t_{ip}$ (s)	$\epsilon_{pass}$ (Sequence A)	$\epsilon_{pass}$ (Sequence B)
1200	1	7.5	0.15	0.41
1160	1	11.5	0.34	0.51
1100	1	12.0	0.49	0.57
1030	5	7.0	0.34	0.52
994	5	5.4	0.35	0.22
951	5	3.9	0.44	0.29
900	5	—	0.54	0.14

### III. RESULTS

#### A. Microstructural Characterization

##### 1. Initial austenite microstructures

Figures 2(a) through (c) shows the austenite microstructures present before  $\gamma \rightarrow \alpha$  phase transformation characterized from the samples quenched at 850 °C following application of different deformation schedules. The figure shows that deformed austenite microstructures are obtained for both steels and deformation schedules, elongated in the plastic flow direction. During roughing simulation, recrystallization is expected to take place at high temperatures and relatively long interpass times, leading to a refinement of the reheated microstructure and the development of equiaxed grains. However, during finishing, the lower temperatures and shorter interpass times in combination with the effect of microalloying elements retarding or even preventing recrystallization,<sup>[23,24,32]</sup> lead to a pancaked microstructure, as observed in Figure 2 in the case of both sequences. However, it is also evident that the lower amount of strain applied during the last finishing

passes in sequence B leads to lower accumulated strain than for sequence A.

##### 2. Transformed microstructures

Figure 3 shows optical micrographs of the transformed microstructures for both steels at different coiling simulation start temperatures (550 °C, 600 °C, 650 °C) and a final cooling rate of 0.03 °C/s. Figures 3(a) through (f) correspond to sequence A and Ti0Nb3 and Ti10Nb3 steels. It can be observed that under these conditions, mainly ferritic microstructures are obtained within the coiling simulation range considered. Some grain refinement is also detected for the Ti10Nb3 steel relative to Ti0Nb3 one. Regarding sequence B and steel Ti10Nb3 (Figures 3(g) through (i)), while at 650 °C coiling simulation start, the microstructure also remains ferritic, as the coiling start temperature decreases to 600 °C or 550 °C, the presence of more acicular phases and greater microstructural heterogeneity can be appreciated. Moreover, in the case of the lowest coiling temperature of 550 °C, the presence of some martensite/austenite (M/A) islands, which were identified by LePera etching, can be observed. Examples of these islands are indicated by the arrows in Figure 3(g). In the case of sequence A, the 500 °C coiling simulation temperature was also studied. At this condition, the microstructure was also mainly ferritic in the case of the Ti0Nb3 steel, while in the case of the Ti10Nb3 steel, it was more acicular with the presence of M/A islands also. Similarly, the analysis of the 0.01 °C/s-Sequence A samples corresponding to the Ti10Nb3 steel after coiling simulation start from 500 °C to 600 °C did not reveal any significant differences with regard to those at 0.03 °C/s.

EBSD scans were also collected from all transformed samples in order to analyze the microstructures more quantitatively. Figure 4 shows examples of grain boundary maps and Figure 5 the corresponding grain size distributions obtained using a tolerance angle of 4 deg misorientation for grain definition for both steels and deformation sequences, at coiling simulation start temperatures of 550 °C and 650 °C (0.03 °C/s final cooling rate). In the maps, the low-angle grain boundaries ( $4^\circ < \theta < 15^\circ$ ) are represented in red and the high-angle grain boundaries ( $\theta > 15^\circ$ ) in black. The differences in the microstructures become more apparent in these figures. Figure 4(a) and (d) shows that in the case of the Ti0Nb3 steel after application of sequence A at both coiling temperatures, an equiaxed microstructure, with a low amount of low-angle grain boundaries, is obtained, accordingly to the more ferritic microstructure observed in Figures 3(a) and (c). On the other hand, in the case of the Ti10Nb3 steel, the amount of

**Table III. Final Cooling Conditions Employed in the Simulations**

Steel	Sequence	Cooling Rate (°C/s)	Coiling Start Simulation Temperature (°C)
Ti0Nb3	A	0.03	500-550-600-650
Ti10Nb3	A	0.03	500-550-600-650
	A	0.01	500-550-600
	B	0.03	550-600-650

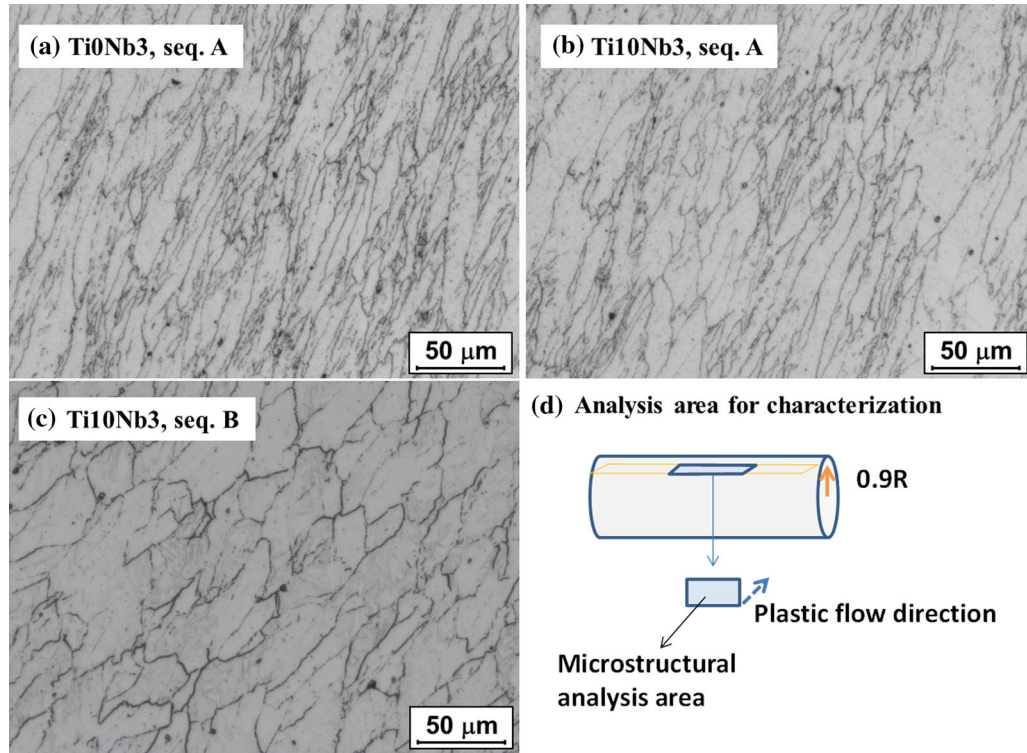


Fig. 2—Austenite microstructures obtained following deformation for (a) Ti0Nb3 steel, Sequence A; (b) and (c) Ti10Nb3 steel, Sequence A and B, respectively. (d) Scheme of the analysis area selected in torsion samples for microstructural characterization.

low-angle grain boundaries significantly increases under the same conditions (Figures 4 (b) and (e)), and this is reflected in the grain refinement observed in Figures 5(b) and (e). However, greater heterogeneity in the size of the areas delimited by high-angle boundaries is detected and, in some cases, these microstructural units show elongated shapes. These last features are more characteristic of bainitic microstructures, although in this case, this is less evident in the optical micrograph (Figure 3(d)). At the temperature of 550 °C, the main effect of application of sequence B on the microstructure of Ti10Nb3 steel (Figures 4(c) and 5(c)) is an increase in grain size and heterogeneity. Increasing the coiling start temperature to 650 °C (Figure 4(d) through (f)) results in more equiaxed and coarser grains, especially in the case of the Ti10Nb3 steel and sequence B condition, as can be observed in the grain size distribution in Figure 5(f).

### B. Hardness Measurements

Hardness measurements were performed in all the transformed samples in order to characterize mechanical behavior, and the results are summarized in Figure 6 as a function of coiling start temperature. It can be noted that for steel Ti10Nb3, higher hardness levels (203 HV to 262 HV) than for steel Ti0Nb3 (164 to 184 HV) were determined. In addition, complex behavior was detected regarding coiling temperature and thermomechanical conditions. In the case of steel Ti10Nb3, sequence A and a cooling rate of 0.03 °C/s, hardness increases with decreasing coiling temperature for all the temperature range considered, while when sequence B is applied, a marked hardness decrease is observed at 650 °C. On the other hand, for the rest of conditions analyzed, a peak in hardness was observed for a given coiling temperature, which varies between 600 °C and 550 °C depending on the sequence being applied and final cooling condition.

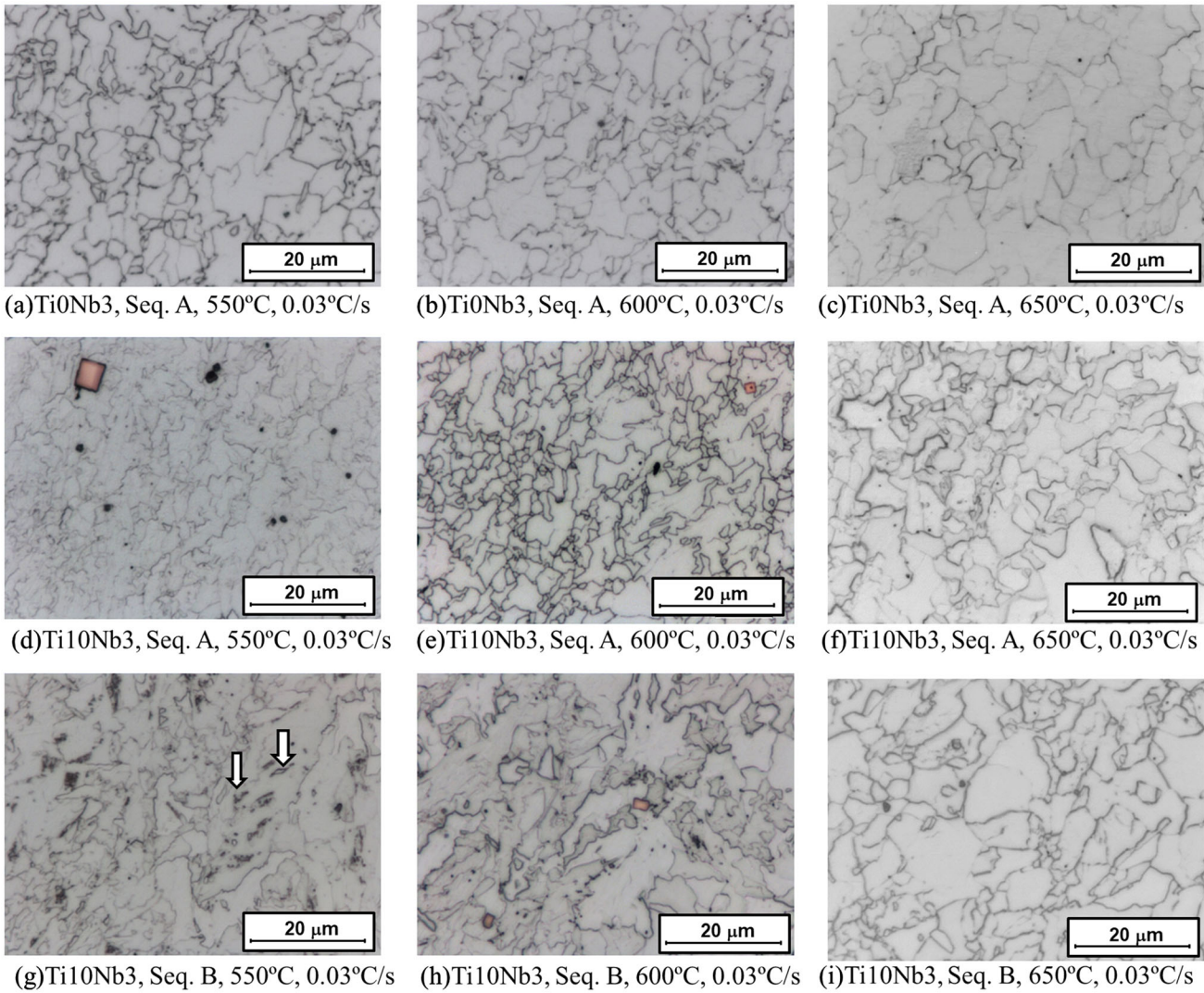


Fig. 3—Examples of transformed microstructures obtained following application of thermomechanical cycle and coiling simulation for Ti0Nb3 steel, Seq. A, 0.03 °C/s: (a) 550 °C, (b) 600 °C, (c) 650 °C; for Ti10Nb3 steel, Seq. A, 0.03 °C/s: (d) 550 °C, (e) 600 °C, (f) 650 °C and for Ti10Nb3 steel, Seq. B, 0.03 °C/s: (g) 550 °C, (h) 600 °C, (i) 650 °C. The arrows in Figure (g) indicate examples of martensite/austenite (M/A) islands.

### C. Precipitation Analysis

To analyze the precipitation state evolution, carbon replicas extracted from specimens quenched at 850 °C corresponding to sequence A, 0.03 °C/s cooling rate, for both steels were first examined. An example of the precipitates found in Ti10Nb3 steel and the corresponding EDS analysis is shown in Figure 7. In accordance with the results obtained from a previous work,<sup>[33]</sup> precipitates coarser than  $\approx 50$  nm that correspond to those undissolved during reheating were found in both samples (Figure 7(a)). According to the EDS analysis of Figure 7(b), both Nb and Ti could be detected in their composition (the presence of Cu and Ni in the EDS analysis arises from the contribution of the specimen holder and grids used to support the replicas). However, as expected, the precipitate density, size, and Ti content in the precipitates were much higher in the Ti10Nb3 steel than in the Ti0Nb3 (in the Ti0Nb3 steel, the Ti content in undissolved precipitates was attributed to the presence of

some residual Ti in its composition). Calculations performed with Thermo-Calc software indicate that, for the Ti10Nb3 steel, less than half of the Ti is available for further precipitation during hot deformation or during/after phase transformation.<sup>[33,34]</sup> In the case of the Ti0Nb3 steel, some particles in the  $\approx 15$  to 30 nm size range, containing only Nb, were also detected. These precipitates are in the size range of strain-induced precipitates that form during deformation sequence,<sup>[35]</sup> although they were scarce. Slightly larger amounts of particles in this size range were found in the Ti10Nb3 steel. An example of these precipitates is shown in Figure 7(c), together with the corresponding EDS analysis (Figure 7(d)). These precipitates contain also Ti and Nb, although in this case, the Ti/Nb ratio is lower than that previously observed for the undissolved particle of Figure 7(a). This is closely in line with the strain-induced precipitate composition described in a previous research,<sup>[33]</sup> where the hot working behavior of high

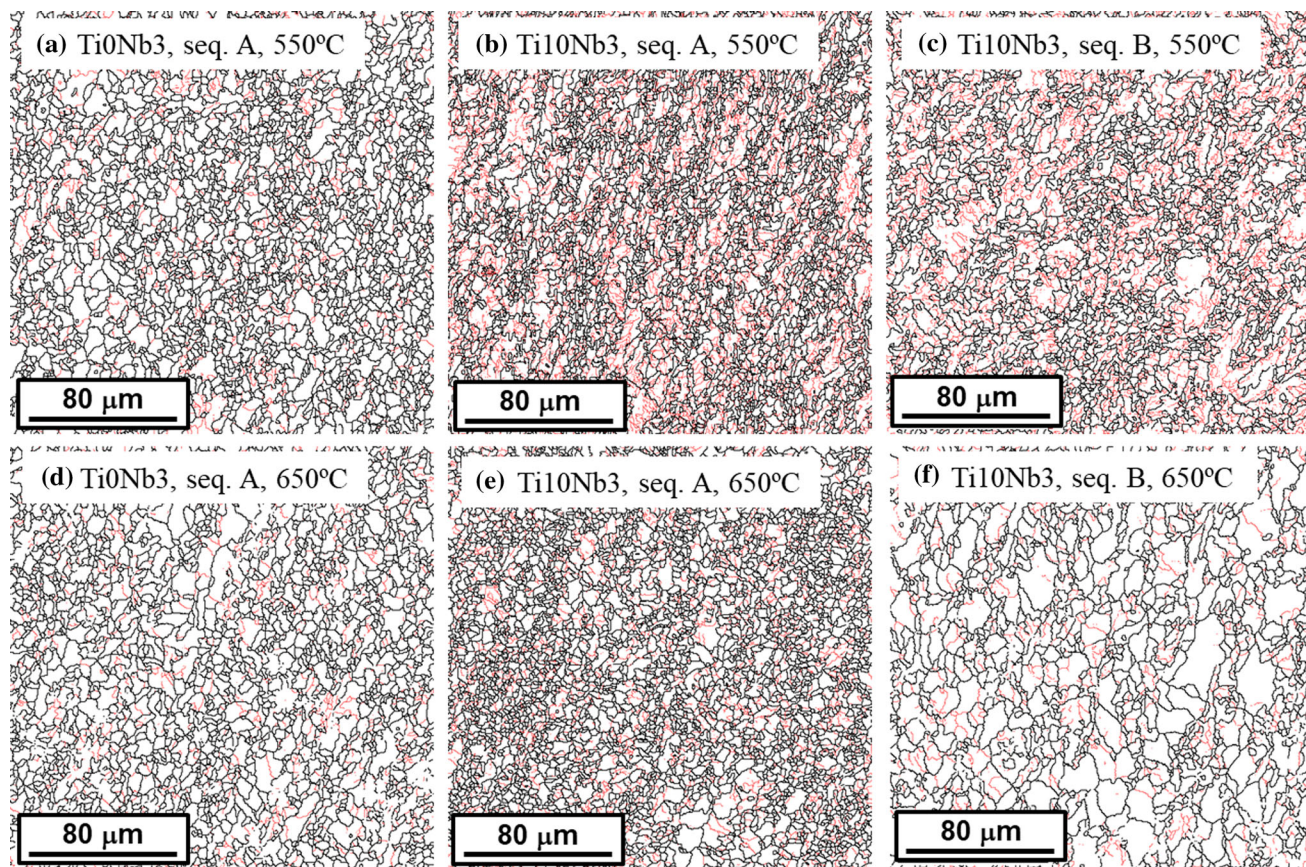


Fig. 4—Grain boundary maps obtained from EBSD scans, with low-angle grain boundaries ( $4^\circ < \theta < 15^\circ$ ) represented in red and high-angle boundaries ( $\theta > 15^\circ$ ) in black for (a) Ti0Nb3, seq. A, 550 °C, (b) Ti10Nb3, seq. A, 550 °C, (c) Ti10Nb3, seq. B, 550 °C, (d) Ti0Nb3, seq. A, 650 °C, (e) Ti10Nb3, seq. A, 650 °C, (f) Ti10Nb3, seq. B, 650 °C, all corresponding to a cooling rate of 0.03 °C/s (Color figure online).

Ti–Nb–microalloyed steels was investigated. Nevertheless, the precipitates were also rather scarce in this sample.

Since the smallest precipitates cannot be reliably identified and their distribution cannot be analyzed in carbon replicas,<sup>[35]</sup> thin foils were prepared from Ti10Nb3 steel samples in order to analyze the precipitates formed during or after phase transformation.

Figure 8 shows representative DF and EFTEM Nb–Ti maps obtained from some of the samples analyzed. Figure 8(a) corresponds to a DF image obtained from sequence A—650 °C coiling condition at the [001] ferrite zone axis, using the (002) reflection of the precipitates as defined by the Baker–Nutting orientation relationship, as shown in Figure 12 in Reference [15]. From the figure, it can be observed that interphase precipitation has occurred, consisting of rows of aligned precipitates formed along with the moving austenite/ferrite boundary during phase transformation. Figure 8(b), (c), and (d) shows Nb–Ti EFTEM representative images obtained at similar magnifications, for sequence A—650 °C, sequence A—600 °C, and sequence B—650 °C, respectively. The precipitate size and density have been quantified in these samples, although the measurements should be taken with care since the amount of material that can be characterized with this

technique is limited. Figure 8(b) confirms that interphase precipitation has taken place in the sequence A—650 °C sample, with an average precipitate size of  $5.7 \pm 0.2$  nm (420 particles measured) and a precipitation density of  $1.1 \times 10^{-5}$  precipitates/nm<sup>3</sup> being measured under these conditions. For the same sequence, at 600 °C coiling, the precipitates were also abundant and, as shown in the figure, in some cases, take on a more needle-like shape. At this temperature, a slightly smaller precipitate size,  $5.2 \pm 0.2$  nm (684 particles measured), was measured, and slightly higher density, namely  $1.4 \times 10^{-5}$  nm<sup>3</sup>. In addition, in this sample, the precipitates no longer seem to be arranged in configurations corresponding to interphase precipitates. Finally, a much larger amount of finer precipitates can be observed in the case of sequence B—650 °C sample (Figure 6(d)). A value of  $3.2 \times 10^{-5}$  precipitates/nm<sup>3</sup> was measured, and they proved to be significantly finer ( $3.1 \pm 0.1$  nm, 1543 particles measured), especially compared to the sequence A—650 °C condition. The large amount of precipitates in this sample made it difficult to discern their configuration, although in some areas of the thin foils, interphase precipitation could also be identified.

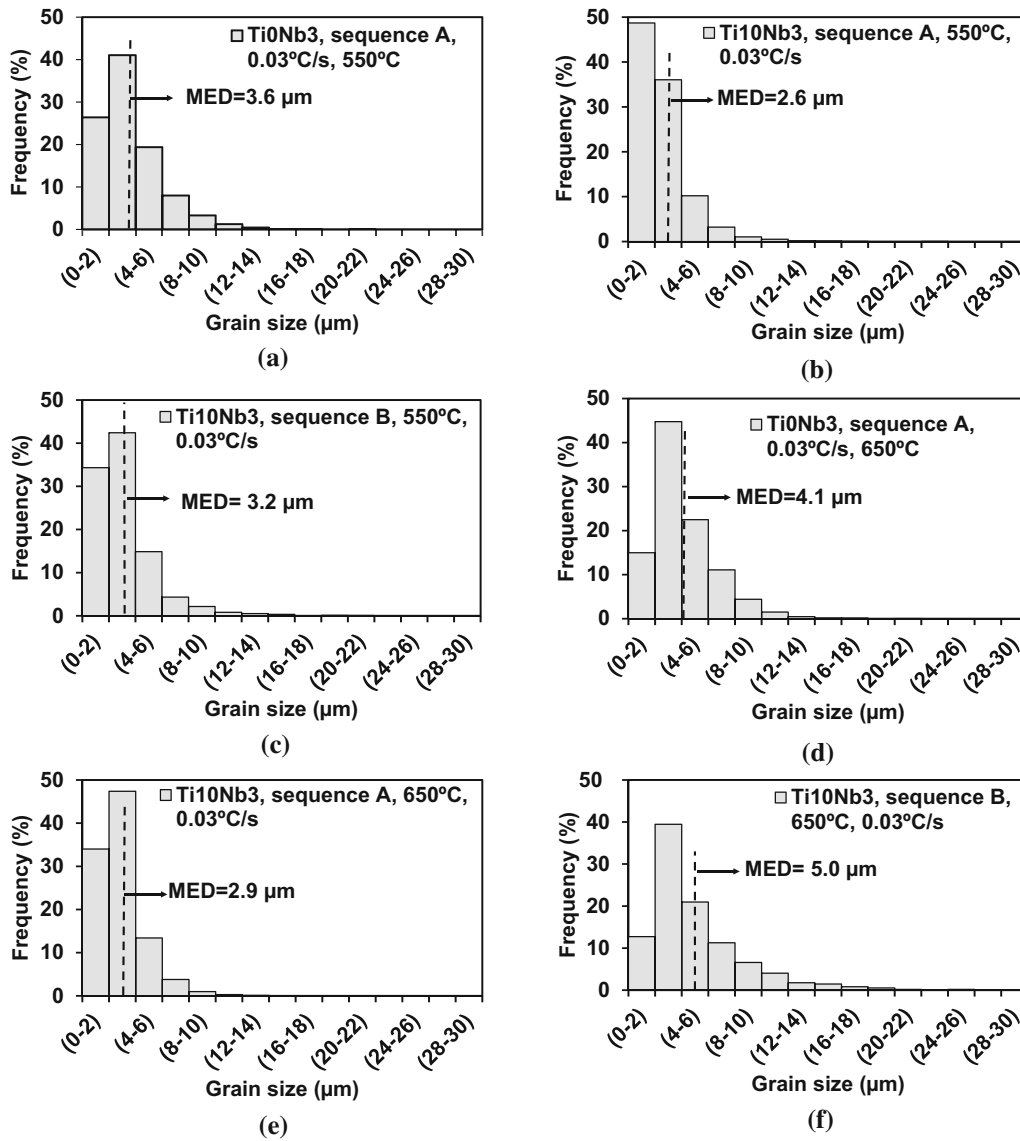


Fig. 5—Grain size distributions corresponding to 4° misorientation angle for grain definition: (a) Ti10Nb3, seq. A, 550°C, (b) Ti10Nb3, seq. A, 550 °C, (c) Ti10Nb3, seq. B, 550 °C, (d) Ti10Nb3, seq. A, 650 °C, (e) Ti10Nb3, seq. A, 650 °C, (f) Ti10Nb3, seq. B, 650 °C, all corresponding to a cooling rate of 0.03 °C/s.

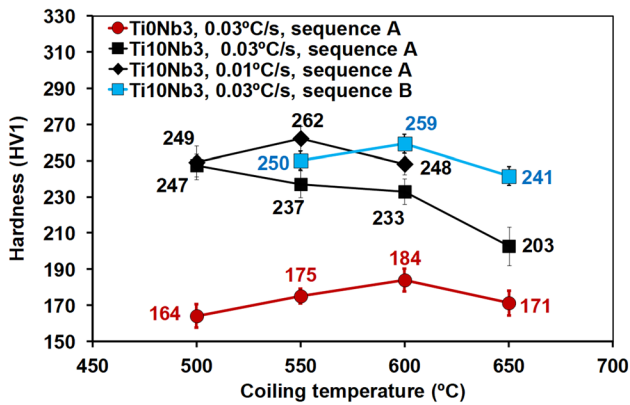


Fig. 6—Hardness determined from the torsion specimens analyzed in this work as a function of coiling simulation temperature.

To further analyze the precipitate configuration in the 0.03 °C/s to 600 °C—sequence A Ti10Nb3 sample, in Figure 9(a), another TEM micrograph obtained at lower magnifications is shown, and in Figure 9(b), an EFTEM Nb–Ti map corresponding approximately to the rectangular area marked in Figure 9(a) is included. Although the map is rather noisy (it was obtained from a thicker foil area than those in Figure 8), it can be observed that higher Nb–Ti concentrations are detected within areas that most likely correspond to defects or dislocations in the microstructure. The results indicate, therefore that in this sample, precipitation is taking place following phase transformation in defects within the ferritic matrix. This explains the elongated shape of some of them, which has also been observed in other works in the case of precipitates formed at dislocations.<sup>[36]</sup> A transition from interphase precipitation at high coiling temperatures to

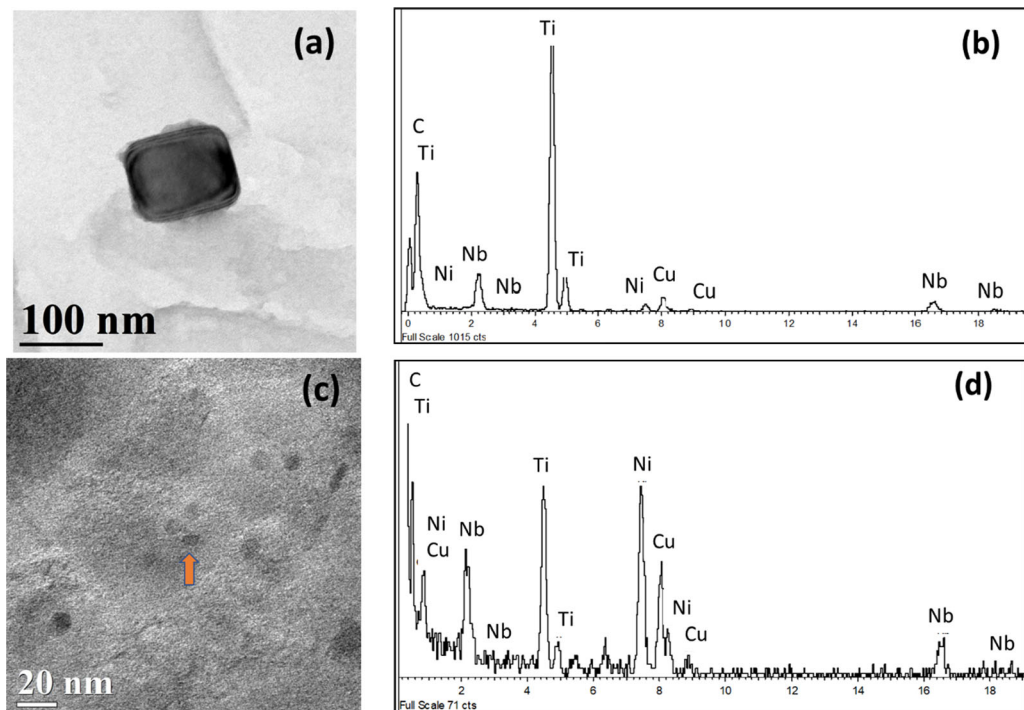


Fig. 7—TEM micrographs showing precipitates found in carbon extraction replicas from Ti10Nb3 specimen, sequence A, 0.03 °C/s cooling rate quenched at 850 °C: (a) undissolved precipitate and (b) its corresponding EDS analysis; (c) strain-induced precipitates and (d) EDS analysis of the precipitate indicated by the arrow in (c).

a more random one with decreasing transformation temperature has also been observed in other works.<sup>[20,37]</sup> A similar analysis was carried out in the sequence B—600 °C samples, and although some very small precipitates were imaged in the thinnest areas of the thin foils, no information could be obtained regarding their configuration.

Regarding the chemical composition of the precipitates formed during or after phase transformation, the small size of these particles makes difficult to adequately perform EDS analysis in thin foils because of the high contribution of the steel matrix. Alternatively, EDS analyses were carried out on carbon replicas prepared from samples after coiling simulations. In Figure 10, an example of these precipitates corresponding to Ti10Nb3 steel, sequence B, 0.03 °C/s cooling rate, and 650 °C coiling temperature simulation is shown. Similar to that observed for undissolved and strain-induced precipitates, particles formed during cooling/coiling stages also contain both Nb and Ti. Although the EDS analysis performed is qualitative, different Ti/Nb ratios can be observed within the different types of precipitates. In most cases, the highest Ti/Nb ratio is found for the undissolved coarse particles formed during solidification, such as the one shown in Figure 7(a). For strain-induced precipitates, Ti/Nb ratio decreases, but it increases again for the small precipitates identified after coiling simulations. These results suggest that the presence of Nb promotes strain-induced precipitation to take place during hot deformation, while at low temperatures during final cooling, Ti is again the major component in the precipitates.

## IV. DISCUSSION

### A. Room-Temperature Microstructures

The austenite microstructures obtained after hot deformation influence the final room-temperature microstructures obtained after phase transformation. For both steels after sequence A, austenite grain size refinement and high strain accumulation levels promote the formation of fine ferritic microstructures over a wide coiling temperature range, from 500 °C to 650 °C for steel Ti10Nb3, and from 550 °C to 650 °C for steel Ti10Nb3. Only for steel Ti10Nb3 after coiling at 500 °C (0.03 °C/s cooling rate), the microstructure appears more bainitic. Unfortunately, from torsion tests, the experimental transformation start or end temperatures cannot be measured. Nevertheless, the well-known role<sup>[38,39]</sup> of austenite grain size refinement and strain accumulation on promoting the nucleation of ferrite and final grain size refinement can be clearly observed here. On the other hand, for sequence B and Ti10Nb3 steel, the combination of coarser austenite grain size and lower strain accumulation results in the formation of more bainitic phases at temperatures of 600 °C or below. Moreover, at 550 °C and 500 °C for the Ti10Nb3 steel, some M/A islands could be detected in the microstructure. When phase transformation takes place at low temperatures or fast cooling rates, some of the austenite can be retained at room temperature, aided by carbon enrichment, and can partially transform to produce M/A constituents,<sup>[40]</sup> as observed in this work. However, as it will be discussed below, the amount of



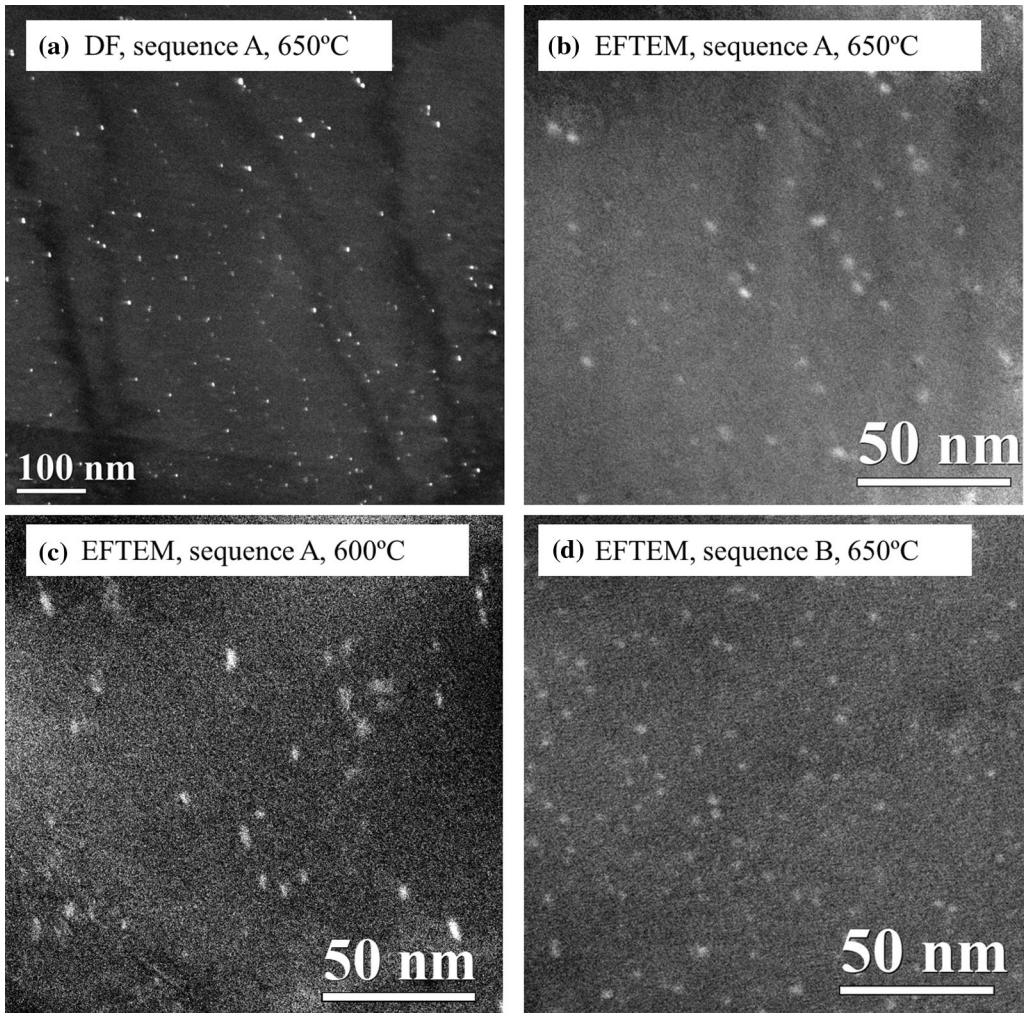


Fig. 8—Dark-field (DF) and Energy-filtered transmission electron microscopy (EFTEM) images from thin foils extracted from Ti10Nb3 samples corresponding to 0.03 °C/s final cooling: (a) DF, sequence A, 650 °C, (b) EFTEM, sequence A, 650 °C, (c) EFTEM, sequence A, 600 °C, (d) EFTEM, sequence B, 650 °C.

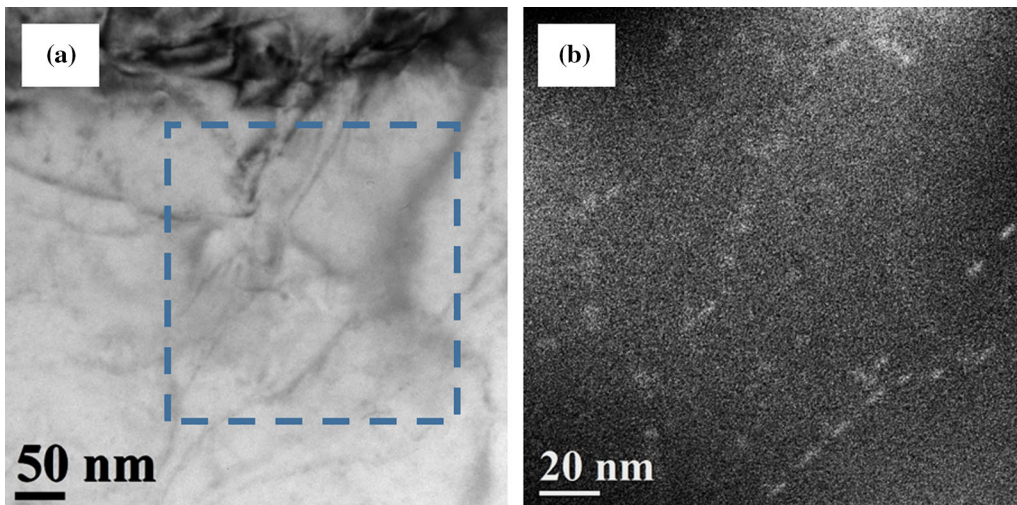


Fig. 9—(a) Bright field (BF) and (b) Nb-Ti EFTEM image obtained approximately from the area marked in (a), corresponding to a thin foil extracted from the Ti10Nb3, 0.03 °C/s cooling, and 600 °C cooling sample.

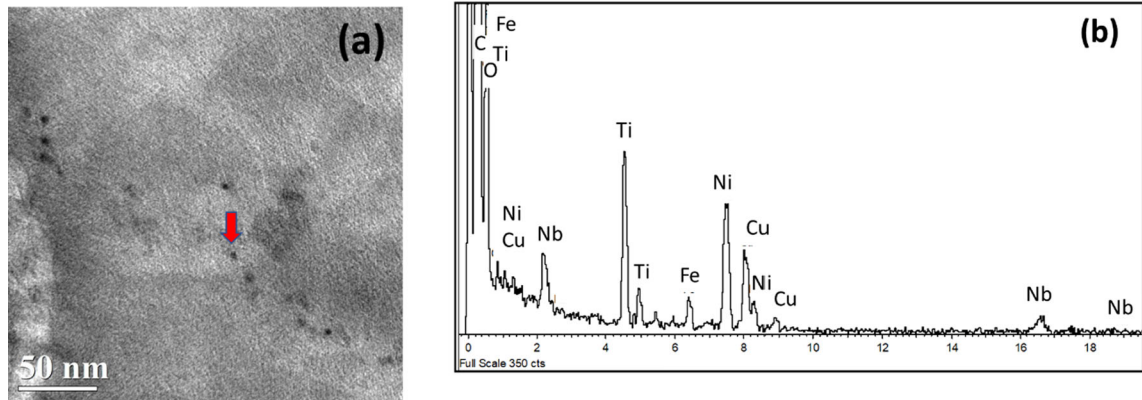


Fig. 10—(a) TEM micrograph from a carbon replica showing a group of small precipitates for the Ti10Nb3 sample after sequence B, 0.03 °C/s cooling rate, 650 °C coiling temperature; (b) EDS analysis of the precipitate marked by the arrow in (a).

these particles is small and only relevant for the coiling temperature of 500 °C (see Table IV).

### B. Mechanical Characterization

As torsion tests have been carried out in this work and conventional tensile tests cannot be easily performed from torsion specimens, mechanical characterization was undertaken using hardness measurements. These hardness values can be converted into *YS* values by applying the following equation determined in a previous work for a group of steels in the same composition range considered in this work<sup>[15]</sup> and close to the rough estimation of  $YS = 3 \cdot HV$ <sup>[41]</sup>:

$$YS[\text{MPa}] = 2.86 \cdot HV - 45.5 \quad [3]$$

Figure 11 summarizes the yield strength results calculated using Eq. [3] for all samples analyzed in this work. In the graph, results obtained in a previous work via dilatometry tests<sup>[15]</sup> have also been included for the Ti10Nb3 steel at comparable roughing, finishing, and coiling simulation conditions. However, it must be pointed out that in dilatometry, the amount of deformation that can be applied is more limited, and therefore, some differences in test conditions and corresponding room-temperature microstructures must be considered:

Using dilatometry, a single deformation pass was applied for roughing ( $\varepsilon = 0.3$ ,  $T = 1100$  °C) and finishing simulation ( $\varepsilon = 0.4$ ,  $T = 900$  °C). Reduced strain led to coarser austenite microstructures and to lower strain accumulation prior to phase transformation than in the present work (compare austenite microstructures from Figure 2 of this paper with those from Figure 1 in Reference 15).

Due to the coarser austenite grain size and more limited strain accumulation in dilatometry samples, hardenability was enhanced and the resulting room-temperature microstructures after coiling were mainly bainitic at temperatures lower than 650 °C. Nevertheless, despite the presence of coarser austenite, the grain sizes ( $4^\circ$  EBSD MED) measured in the transformed

microstructures using dilatometry (from 3.5 to 5.7  $\mu\text{m}$  for coiling temperatures from 550 °C to 650 °C) were comparable to those measured in the present work, although microstructural heterogeneity was clearly greater in dilatometry samples.

As expected from the hardness results, Figure 11 shows that the highest estimated *YS* values were obtained for the Ti10Nb3 steel, under some conditions 300 MPa higher than those determined for the Ti0Nb3 steel. However, it can also be noted that the coiling temperatures corresponding to the highest *YS* values are not only dependent on cooling rate and steel composition but also on the previous austenite condition. In the case of the Ti10Nb3, the highest estimated *YS* values were determined in the dilatometry samples for coiling temperatures between 625 °C and 650 °C. Yield strengths between 745 and 754 MPa were calculated under these conditions. On the other hand, in the torsion tests, the maximum *YS* values attained are lower and obtained at lower coiling temperatures: at 600 °C for sequence B—0.03 °C/s (696 MPa), at 550 °C for sequence A—0.01 °C/s (705 MPa), and at the lowest coiling temperature, 500 °C, for sequence A—0.03 °C/s (662 MPa).

### C. Analysis of Strengthening Mechanisms

The results show that, as well as final cooling conditions, the deformation sequence can also affect hardness significantly, and consequently, the mechanical properties that can be obtained for a given steel and deformation sequence. An additive contribution has been proposed as the most suitable to describe the dependence of yield strength (*YS*) on the different strengthening mechanisms<sup>[42,43]</sup>:

$$YS = \sigma_0 + \sigma_{ss} + \sigma_{iss} + \sigma_{HP} + \sigma_{disloc} + \sigma_{prec} + \sigma_{M/A}, \quad [4]$$

where  $\sigma_0$  is the friction stress,  $\sigma_{ss} + \sigma_{iss}$  the stresses produced by substitutional and interstitial elements in solid solution, and  $\sigma_{HP}$  the grain size strengthening contribution. For low transformation temperatures, more displacive phases can form and the effect of

**Table IV. M/A Particle Size and Volume Fraction Measurements and Calculated Strengthening Contribution for Ti10Nb3 Samples**

Seq.	Condition	N <sup>o</sup> Measurements	MED (μm)	f <sub>M/A</sub>	σ <sub>M/A</sub> (MPa)
A	500 °C to 0.01 °C/s	1745	0.54 ± 0.01	0.003	3
	550 °C to 0.01 °C/s	1570	0.50 ± 0.01	0.002	2
	500 °C to 0.03 °C/s	5621	0.78 ± 0.01	0.020	18
B	550 °C to 0.03 °C/s	961	0.28 ± 0.04	0.003	3

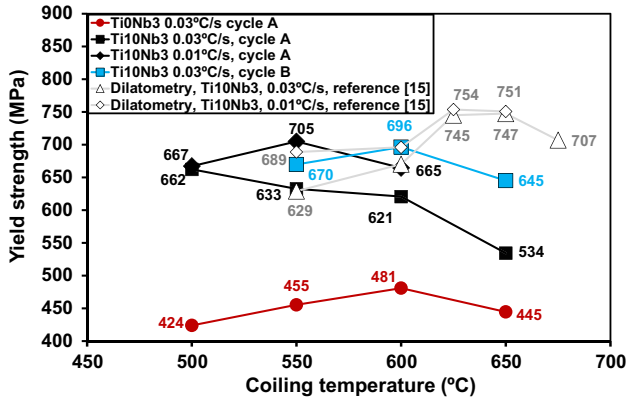


Fig. 11—Yield strength estimated from hardness data obtained from the samples analyzed in this work, and for the Ti10Nb3 steel via dilatometry in a previous work<sup>[15]</sup>.

increased dislocation density,  $\sigma_{\text{disloc}}$ , should also be taken into account. A strengthening contribution from precipitates,  $\sigma_{\text{prec}}$ , can be obtained in microalloyed steels and, if M/A islands are present, their strengthening contribution ( $\sigma_{\text{M/A}}$ ) may also be relevant.

The following equation has been applied to calculate the contribution made by friction stress and substitutional elements to  $YS$ <sup>[43,44]</sup>:

$$\sigma_0 + \sigma_{\text{ss}}[\text{MPa}] = 54 + 32[\text{Mn}] + 83[\text{Si}] + 678[\text{P}] + 39[\text{Cu}] - 31[\text{Cr}] + 11[\text{Mo}], \quad [5]$$

where the composition of all elements is given in wt pct. Regarding the effect of interstitial elements, after coiling, the amount of C remaining in solution can be considered negligible, while the effect of free N can be estimated as follows<sup>[43]</sup>:

$$\sigma_{\text{iss}}[\text{MPa}] = 5000[\text{N}_{\text{free}}] \quad [6]$$

with  $\text{N}_{\text{free}}$  referring to the amount of N (wt pct) in solid solution at room temperature. In the case of the Ti10Nb3 steel, all the N is expected to be pinned in coarse Ti precipitates that remain undissolved during reheating, and therefore, the contribution of free N can be ignored in this steel. As a result, while equation (5) yields very close values of  $\sigma_0 + \sigma_{\text{ss}} = 127$  MPa for both Ti0Nb3 and Ti10Nb3 steels, in the case of Ti0Nb3 steel, considering that all the N remains free, a slightly higher value of  $\sigma_0 + \sigma_{\text{ss}} + \sigma_{\text{iss}} = 145$  MPa has been determined.

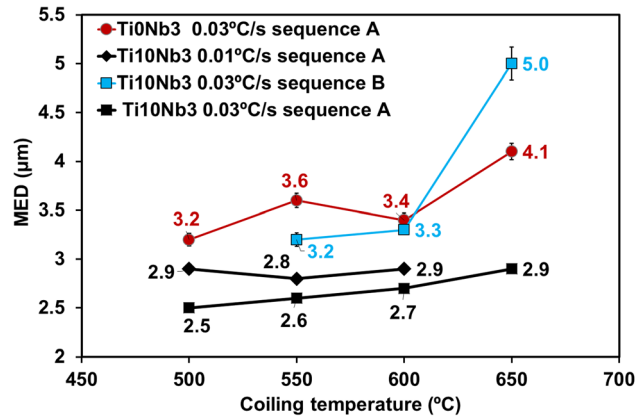


Fig. 12—(a) Grain sizes measured via electron backscatter diffraction (EBSD) in terms of mean equivalent diameter (MED) for all samples analyzed using 4° tolerance for grain boundary definition.

The strengthening effect of grain boundaries can be calculated as follows<sup>[45]</sup>:

$$\sigma_{\text{HP}}[\text{MPa}] = k_{\text{HP}} \cdot d^{-0.5} \quad [7]$$

with  $k_{\text{HP}}$  values that are usually between 15 and 18  $\text{MPa} \cdot \text{mm}^{0.5}$  (a value of  $17.4 \text{ MPa} \cdot \text{mm}^{0.5}$  has been considered in this work<sup>[43,44]</sup>) and  $d$  the ferrite grain size in mm determined using the mean linear intercept (MLI) parameter measured by optical microscopy. In a previous work,<sup>[44]</sup> comparison of the mean equivalent diameter (MED) calculated from EBSD and the MLI values determined by optical microscopy in ferritic microstructures showed that both parameters were most comparable when a tolerance angle was applied in EBSD for grain boundary definition of 4 deg. The grain sizes determined by EBSD in this work using this criterion are summarized in Figure 12. It can be observed that, in all cases, the finest grain sizes were determined for the Ti10Nb3 steel deformed following sequence A and final cooling at 0.03 °C/s. Under these conditions, the grain sizes tend to slightly decrease from 2.9 to 2.5 μm with decreasing coiling temperature from 650 °C to 500 °C. When a slower cooling rate of 0.01 °C/s is applied, slightly coarser grain sizes are determined, very close to 2.9 μm for coiling simulation temperatures between 600 °C and 550 °C. In the case of the Ti0Nb3 steel, sequence A and cooling at 0.03 °C/s, the MED values are coarser, ranging from 4.1 μm at 650 °C to 3.2 μm at 500 °C. Grain sizes in the same

range are obtained for the Ti10Nb3 steel when sequence B and 0.03 °C/s final cooling are applied, except for the highest coiling temperature condition considered (650 °C). At this temperature, the grain size increase is larger and the coarsest value is measured accordingly (5.0 μm).

Regarding dislocation density strengthening, according to Taylor's equation, this can be calculated as follows:

$$\sigma_{\text{disloc}} = \alpha M \mu b \sqrt{\rho}, \quad [8]$$

where  $\alpha$  is a constant,  $M$  the average Taylor factor, and  $\mu$  the shear modulus (a value of  $\alpha M \mu b = 7.34 \cdot 10^{-6}$  MPa·m was considered following<sup>[43]</sup>). In several works, the dislocation density ( $\rho$ ) has been estimated from EBSD results as follows<sup>[46]</sup>:

$$\rho = 2\theta/(ub) \quad [9]$$

where  $u$  is the unit length,  $\theta$  the Kernel average misorientation, and  $b$  the Burgers vector magnitude ( $b = 2.5 \times 10^{-10}$  m). The Kernel average misorientation data, determined using misorientation values lower than 2 deg<sup>[20,44]</sup> and the first neighbor criterion, as well as the corresponding dislocation density values calculated using equation (9), are represented in Figure 13. As can be observed, dislocation density values from  $2.3 \times 10^{14} \text{ m}^{-2}$  to  $1.13 \times 10^{14} \text{ m}^{-2}$  were calculated using this approach. Values in this range have also been reported in other works for Nb or Nb-high Ti-microalloyed steels.<sup>[20,33,44,47]</sup> As the figure shows, the lowest values of  $\theta$ , between 0.49° and 0.63°, were determined for the Ti10Nb3 steel, with no clear dependence on coiling temperature. The low  $\theta$  values determined are closely in line with the ferritic aspect of the microstructures observed by optical microscopy and EBSD (Figures 3 and 4). However, it should be mentioned that these low  $\theta$  values are also within the range of error expected from EBSD measurements and, under these conditions, application of this methodology can lead to an overestimation of the dislocation-strengthening contribution.<sup>[44]</sup> In the case of the Ti10Nb3 steel, the  $\theta$

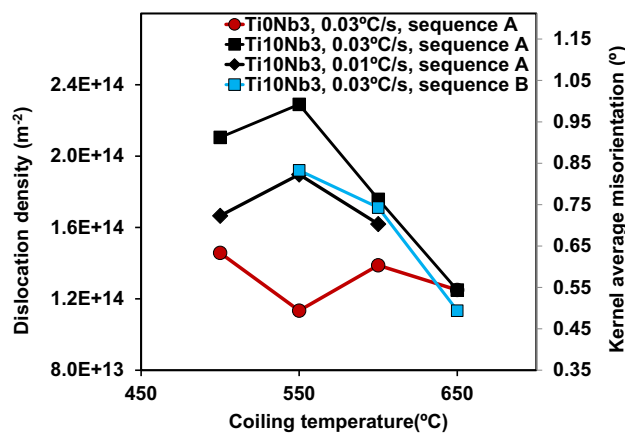


Fig. 13—Kernel average misorientation and dislocation density values calculated using equation (9) for the samples analyzed.

values are also within this range for both sequences and cooling rates at 650 °C. However, at lower coiling temperatures of 600 °C and 550 °C,  $\theta$  increases and tends to stabilize at the lowest coiling temperature of 500 °C. It should be noted that the dislocation density increase at low coiling temperatures is slightly more marked for sequence A and 0.03 °C/s cooling rate than for sequence B or for the lower final cooling rate of 0.01 °C/s.

Finally, as mentioned above, the presence of M/A islands was detected in some of the samples. To analyze their effect on mechanical strength, the volumetric fraction of these particles ( $f_{M/A}$ ) was measured using LePera etching in samples in which their presence was considered significant, and their contribution to strength estimated as follows<sup>[20,48]</sup>:

$$\sigma_{M/A} = 900f_{M/A}. \quad [10]$$

The results of the analysis are summarized in Table IV. As can be observed, in all cases, the size, volume fraction, and calculated contributions to the yield strength are quite low. The most relevant hardening contribution was determined for the Ti10Nb3 steel, sequence A—500 °C—0.03 °C/s sample ( $\approx 20$  MPa).

The calculated microstructural-strengthening contributions have been summarized for the samples analyzed in this work in Figure 14. Regarding dislocation strengthening, as mentioned above, in many cases, low  $\theta$  values were determined, within the error range for the equipment, and the same approach employed in a previous work<sup>[44]</sup> has been applied in order to take this into account, i.e., all calculated dislocation density values were corrected by subtracting from them the value corresponding to the lowest dislocation density (Ti10Nb3, sequence B, 0.03 °C/s, 650 °C,  $\theta = 0.49$  deg). The approach is based on the fact that, in Pickering's original equation, the dislocation density inherent to ferritic samples is included. As measurement of precipitation-strengthening contribution is rather complicated, this was estimated as the difference between experimental YS values and the rest of the contributions. Figure 14(a) shows that for both steels, grain size strengthening is the most relevant contribution to yield strength at all the coiling temperatures, as already observed in steels with similar composition.<sup>[15,20]</sup> In general, some increase in grain size contribution with decreasing coiling temperature was observed, while the variations in precipitation and dislocation-strengthening contributions differ significantly depending on the steel and processing conditions. In the case of the Ti10Nb3, dislocation and precipitation-strengthening contributions are small.

In the case of the Ti10Nb3 steel, dislocation-strengthening contributions are greater and in general increase with decreasing coiling temperature, although for the 0.01 °C/s sequence A samples, a maximum is observed at 550 °C. Regarding precipitation strengthening, its contribution is also much greater in this steel than for the Ti0Nb3, closely in line with previous results,<sup>[15]</sup> and also within the range reported in other researches.<sup>[8,20]</sup>

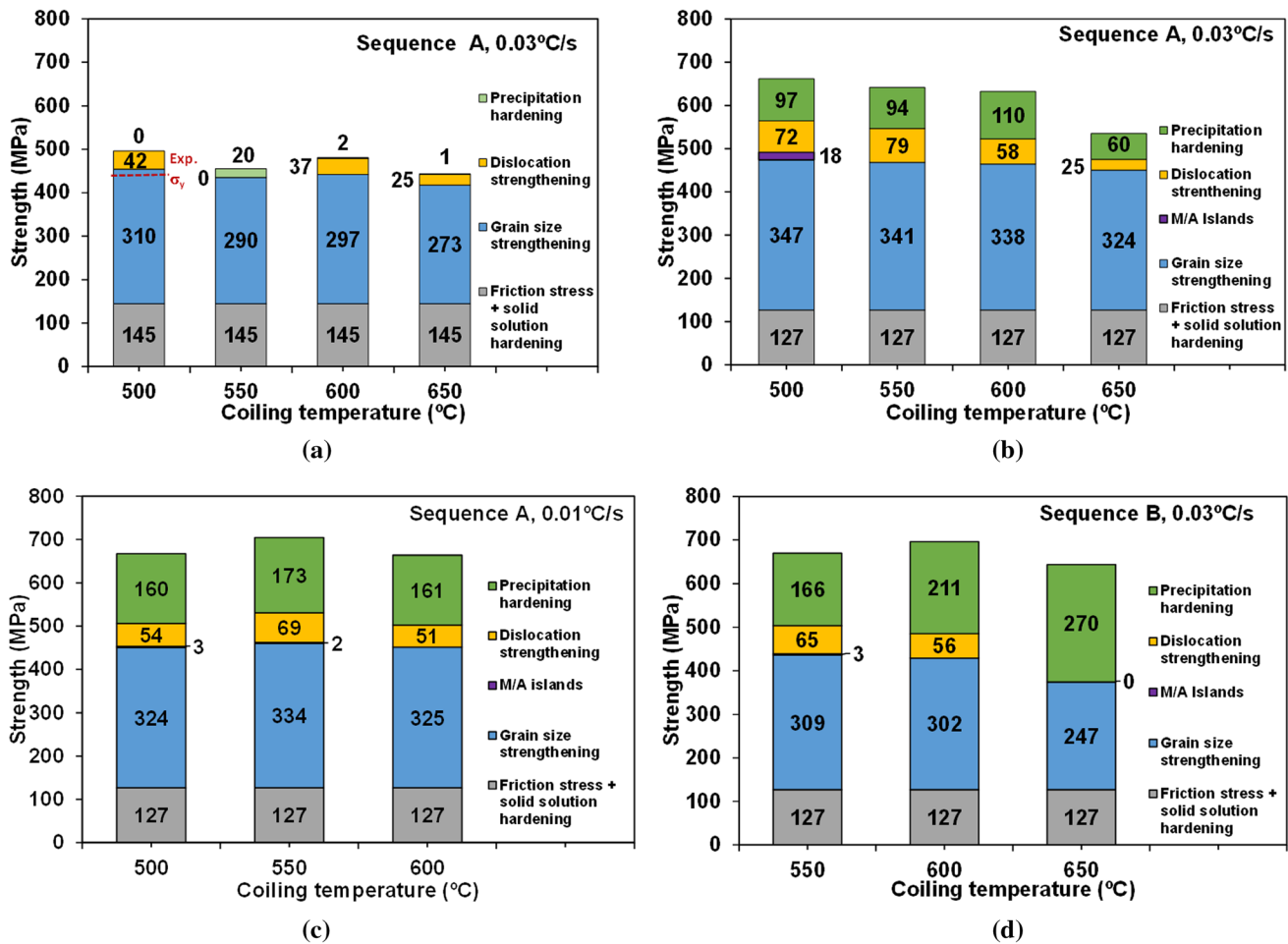


Fig. 14—Calculated strengthening mechanisms for the samples analyzed in this work: (a) Ti0Nb3 steel, Seq. A, 0.03 °C/s; (b) Ti10Nb3 steel, Seq. A, 0.03 °C/s; (c) Ti10Nb3, Seq. A, 0.01 °C/s; and (d) Ti10Nb3 steel, Seq. B, 0.03 °C/s. The numbers represent the individual contribution of each mechanism in MPa.

Comparing Figures 14(b) and (d), it can be observed that for the same cooling rate of 0.03 °C/s, the contribution made by precipitation is much greater for sequence B than for sequence A. Different trends can be observed depending on the condition analyzed. For sequence A—0.03 °C/s, the lowest value was determined at the highest coiling temperature, 650 °C (60 MPa), while below this temperature, it slightly increases and stabilizes at  $\approx 100$  MPa. For the same sequence A, reducing the final cooling rate to 0.01 °C/s, precipitation contributions significantly increase, reaching the maximum (173 MPa) at 550 °C. On the other hand, for sequence B—0.03 °C/s, the maximum contribution was obtained at the highest coiling temperature (650 °C) and decreases continuously from 270 to 166 MPa as coiling temperature decreases from 650 °C to 550 °C. This behavior is in line with that observed in dilatometry simulations,<sup>[15]</sup> i.e., precipitation contributions also decreased as coiling temperature decreased, although in that case, much higher values were observed above 600 °C, ranging between 240 and 307 MPa.

One of the reasons that might explain the lower precipitation strengthening determined in this work compared to dilatometry tests is that application of the multipass thermomechanical sequence could enhance strain-induced precipitation occurrence during austenite hot deformation. This may, therefore, result in some loss of the microalloying element content available for precipitation during or after phase transformation, especially for sequence A, where strain accumulation is higher. However, although some effect of this loss of microalloying element in solid solution cannot be excluded, the amount of strain-induced precipitates detected via TEM in quenched samples from sequence A was scarce, as mentioned above.

Another effect of higher strain accumulation is to increase the phase transformation start and finish temperatures.<sup>[49]</sup> This implies that, following application of sequence A, phase transformation is expected to take place at temperatures higher than in cycle B or in dilatometry simulations, which means that the precipitation that takes place during phase transformation, or even after, also takes place at higher temperatures. The

effect of temperature on precipitation is a complex one. As temperature decreases, the driving force for precipitation nucleation increases, while microalloying element diffusivity in turn decreases.<sup>[50]</sup> Classical nucleation theory predicts that, at high precipitation temperatures, nucleation of a larger amount of precipitates takes place as temperature decreases due to increased driving force. In addition, this is accompanied by lower growth potential due to reduced microalloying element diffusivity. However, below a certain temperature, nucleation rate decreases due to reduced diffusivity, leading to the formation of fewer precipitates of smaller size.

In the case of sequence A, at least at high coiling temperatures, above shown experimental TEM results of average precipitate size and density indicate that higher transformation temperatures promote precipitation of a lower volume fraction of precipitates of coarser size compared to sequence B, with both factors helping to reduce precipitation strengthening.<sup>[51]</sup>

In the case of the dilatometry specimens, at 650 °C, very small precipitates were identified, < 3 nm, (see Figure 12 in Reference 15), which supports the high precipitate-strengthening contribution calculated under these conditions, 299 Mpa.<sup>[15]</sup> Reducing the coiling temperature, precipitation contribution decreases, probably due to a reduction in the amount of particles that can precipitate at lower temperatures, although the values remain high (139 and 100 MPa at 600 °C and 550 °C, respectively). The same occurs in the case of sequence B, albeit to a lesser extent. On the other hand, for sequence A at 0.03 °C/s, cooling rate precipitation strengthening increases when reducing the coiling temperature from 650 °C to 600 °C, closely in line with TEM results: slightly lower precipitate size was measured at 600 °C ( $5.2 \pm 0.2$  nm) than at 650 °C ( $5.7 \pm 0.2$  nm), while precipitate density was slightly higher ( $1.4 \times 10^{-5}$  vs  $1.1 \times 10^{-5}$  precipitates/nm<sup>3</sup>). Under these conditions, a transition from interphase to precipitation at dislocations was observed, which makes it difficult to compare both situations. In the case of sequence B, it is not possible to analyze whether this transition takes place due to the smaller size of the precipitates that form compared to sequence A. However, it is worth noting that, although it decreases as temperature decreases, precipitation hardening also remains higher at lower temperatures for sequence B than for sequence A.

In the case of the sequence A—0.03 °C/s condition, the maximum *YS* was determined at the lowest coiling temperature considered, 500 °C. Under this condition, grain size, precipitation, and dislocation-strengthening contributions are quite similar to those determined at 550 °C. However, the fact that the highest fraction of M/A particles was detected in this sample must be taken into account, and although application of equation (8) yields rather low M/A strengthening (18 MPa), this effect might be greater than estimated.

Regarding 0.01 °C/s condition, precipitation analysis was not performed. However, reducing the cooling rate means a longer time at precipitation temperature range, which is expected to lead to the formation of a larger

amount of precipitates than for the 0.03 °C/s final cooling rate samples, which explains the greater strengthening observed.

Finally, it is also worth noting that, for the conditions considered, maximum *YS* values were obtained for dilatometry tests at coiling temperatures between 625 °C and 675 °C. However, it should also be noted that the microstructure in these samples, transformed from coarsest austenite with lowest strain accumulation, was significantly more heterogeneous, this having a possible impact on other mechanical properties, such as toughness. The same considerations may be applied when comparing the microstructures obtained following sequence B and A.

## V. CONCLUSIONS

- The much higher *YS* values achieved with high Ti addition to a Nb-microalloyed steel are mainly due to an increase in precipitation hardening, in some cases over 300 MPa. Nevertheless, this strengthening mechanism shows a major dependence on deformation sequence and final cooling conditions.
- For the Ti–Nb steel, the lowest precipitation-strengthening contributions (between 60 and 110 MPa) were obtained after applying sequence A, which leads to the highest strain accumulation level, and cooling at 0.03 °C/s. For this sequence, decreasing the final cooling rate to 0.01 °C/s results in an increase in precipitation strengthening at all coiling temperatures ( $\approx 160$  to 170 MPa). On the other hand, for sequence B, with less strain accumulation, the precipitation-strengthening values increase significantly, ranging from 166 to 270 MPa with increasing coiling temperature from 550 °C to 650 °C. Results obtained in a previous work via dilatometry with the same high Ti–Nb steel under comparable conditions but even lower austenite strain accumulation show a similar dependence, with even greater precipitation strengthening at high coiling temperatures.
- The lower precipitation strengthening obtained for the sequence A is mainly related to the promotion of higher phase transformation start and end temperatures. This results in a lower driving force for precipitation nucleation during or after phase transformation and higher microalloying element diffusivity. As a result, at high coiling temperatures, fewer and coarser precipitates are formed, both factors tending to reduce precipitation strengthening.
- As a result of the differences in precipitation strengthening, in the case of the high Ti–Nb steel, the coiling temperature corresponding to highest *YS* also depends on deformation sequence and the final cooling condition. As for the high strain accumulation sequence A and 0.03 °C/s, this occurs at 500 °C; when reducing the cooling rate to 0.01 °C/s, it shifts to 550 °C, and in the case of sequence B with lower strain accumulation and 0.03 °C/s, this takes place at

600 °C. This indicates that for a given cooling rate, the coiling temperature leading to the highest  $\dot{\gamma}$  moves to lower values with increasing the accumulated strain.

## ACKNOWLEDGMENTS

The authors acknowledge the RCFS project no. RFSR-CT-2015-00013 for financial support.

## CONFLICT OF INTEREST

The authors declare that they have no conflict of interest.

## FUNDING

Open Access funding provided thanks to the CRUE-CSIC agreement with Springer Nature.

## OPEN ACCESS

This article is licensed under a Creative Commons Attribution 4.0 International License, which permits use, sharing, adaptation, distribution and reproduction in any medium or format, as long as you give appropriate credit to the original author(s) and the source, provide a link to the Creative Commons licence, and indicate if changes were made. The images or other third party material in this article are included in the article's Creative Commons licence, unless indicated otherwise in a credit line to the material. If material is not included in the article's Creative Commons licence and your intended use is not permitted by statutory regulation or exceeds the permitted use, you will need to obtain permission directly from the copyright holder. To view a copy of this licence, visit <http://creativecommons.org/licenses/by/4.0/>.

## REFERENCES

1. M.A. Altuna, A. Iza-Mendia, and I. Gutierrez: *Metall. Mater. Trans. A.*, 2012, vol. 43A, pp. 4571–86. <https://doi.org/10.1007/s11661-012-1270-x>.
2. S.F. Medina, M. Chapa, P. Valles, A. Quispe, and M.I. Vega: *ISIJ Int.*, 1999, vol. 39, pp. 930–6. <https://doi.org/10.2355/isijinternational.39.930>.
3. S. Freeman and R.W.K. Honeycombe: *Met. Sci.*, 1977, vol. 11, pp. 59–64. <https://doi.org/10.1179/msc.1977.11.2.59>.
4. R.W.K. Honeycombe and R.F. Mehl: *Metall. Mater. Trans.*, 1976, vol. 7, pp. 915–36. <https://doi.org/10.1007/BF02644057>.
5. Y. Funakawa, T. Shiozaki, and K. Tomita: *ISIJ Int.*, 2004, vol. 44, pp. 1945–51. <https://doi.org/10.2355/isijinternational.44.1945>.
6. Y. Funakawa: *ISIJ Int.*, 2019, vol. 60, pp. 2086–95. <https://doi.org/10.2320/matertrans.M2018197>.
7. V.S.A. Challa, W.H. Zhou, R.D.K. Misra, R. O'Malley, and S.G. Jansto: *Mat. Sci. Eng.*, 2014, vol. 59SA, pp. 143–53. <https://doi.org/10.1016/j.msea.2013.12.002>.
8. F.Z. Bu, X.M. Wang, S.W. Yang, J. Shang, and R.D.K. Misra: *Mat. Sci. Eng. A.*, 2015, vol. 620, pp. 22–9. <https://doi.org/10.1016/j.msea.2014.09.111>.
9. C. Chen, J. Yang, C. Chen, and S. Cheng: *Mater. Character.*, 2017, vol. 114, pp. 18–9. <https://doi.org/10.1016/j.matchar.2016.01.023>.
10. J. Chen and G. Wang: *Steel Res.*, 2015, vol. 86, pp. 821–24. <https://doi.org/10.1002/srin.201400275>.
11. I. Timokhina, M.K. Miller, J. Wang, H. Beladi, P. Cizek, and P.D. Hodgson: *Mater. Des.*, 2016, vol. 111, pp. 222–29. <https://doi.org/10.1016/j.matdes.2016.08.086>.
12. R. Ueomori, R. Chijiwa, H. Tamehiro, and H. Morikawa: *Appl. Surf. Sci.*, 1944, vol. 76–77, pp. 255–60. [https://doi.org/10.1016/0169-4332\(94\)90351-4](https://doi.org/10.1016/0169-4332(94)90351-4).
13. J.H. Jang, C.H. Lee, Y.U. Heo, and D.W. Suh: *Acta Mater.*, 2012, vol. 60, pp. 208–17. <https://doi.org/10.1016/j.actamat.2011.09.051>.
14. X. Mao, X. Huo, X. Sun, and Y. Chai: *J. Mater. Process. Technol.*, 2010, vol. 210, pp. 1660–66. <https://doi.org/10.1016/j.jmatprotec.2010.05.018>.
15. L. Garcia-Sesma, B. Lopez, and B. Pereda: *Mater. Sci. Eng. A.*, 2019, vol. 748, pp. 386–95. <https://doi.org/10.1016/j.msea.2019.01.105>.
16. P.K. Patra, S. Sam, M. Singhai, S.S. Hazra, G.D.J. Ram, and S.R. Bakshi: *Trans. Indian Inst. Metals.*, 2017, vol. 70, pp. 1773–81. <https://doi.org/10.1007/s12666-016-0975-8>.
17. B. Okamoto, A. Bogerstram, and J. Agren: *Acta Mater.*, 2010, vol. 58, pp. 4783–90. <https://doi.org/10.1016/j.actamat.2010.05.014>.
18. H.W. Yen, P.Y. Chen, C.Y. Huang, and J.R. Yang: *Acta Mater.*, 2011, vol. 59, pp. 6264–74. <https://doi.org/10.1016/j.actamat.2011.06.037>.
19. V.V. Natarajan, V.S.A. Challa, R.D.K. Misra, D.M. Sidorenko, and M.D. Mulholand: *Mater. Sci. Eng. A.*, 2016, vol. 669A, pp. 1–9. <https://doi.org/10.1016/j.msea.2016.04.007>.
20. G. Larzabal, N. Isasti, J.M. Rodriguez-Ibabe, and P. Uranga: *Metals*, 2017, vol. 7. <https://doi.org/10.3390/met7020065>.
21. S. Tsai, T. Su, J. Yang, C. Chen, Y. Wang and C. Huang: *Mater. Des.*, 2017, pp. 319–25. <https://doi.org/10.1016/j.matdes.2017.01.071>.
22. X. Li, F. Li, Y. Cui, B. Xiao, and X. Wang: *Mater. Sci. Eng. A.*, 2016, vol. 677, pp. 340–48. <https://doi.org/10.1016/j.msea.2016.09.070>.
23. S.S. Hansen, J.B. Vander Sande, and M. Cohen: *Metall. Mater. Trans. A.* 1980, vol. 11A, pp. 387–402. <https://doi.org/10.1007/BF02654563>.
24. S. Vervynck, K. Verbeken, B. Lopez, and J.J. Jonas: *Int. Mater. Rev.*, 2013, vol. 57, pp. 187–207. <https://doi.org/10.1179/1743280411Y.0000000013>.
25. K.B. Kang, O. Kwon, W.B. Lee, and C.G. Park: *Ser. Mater.*, 1997, vol. 36, pp. 1303–8. [https://doi.org/10.1016/S1359-6462\(96\)00359-4](https://doi.org/10.1016/S1359-6462(96)00359-4).
26. B. Pereda, J.M. Rodriguez-Ibabe, and B. Lopez: *ISIJ Int.*, 2008, vol. 48, pp. 1467–556. <https://doi.org/10.2355/isijinternational.48.1457>.
27. Glover and G. Sellars: *Metall. Mater. Trans. B*, vol. 765-775B, 1973, pp. 765–75. <https://doi.org/10.1007/BF02643086>.
28. S. Bechet and L. Beaujard: *Rev. Met.*, 1952, vol. 52, pp. 830–6. <https://doi.org/10.1051/metal/19552100830>.
29. S.I. Wright: *Mater. Sci. Technol.*, 2006, vol. 22, pp. 1287–96. <https://doi.org/10.1179/174328406X130876>.
30. P. Thomas and P.A. Midgley: *Top. Catal.*, 2002, vol. 21, pp. 109–38. <https://doi.org/10.1023/A:1021377125838>.
31. E. Courtois, T. Epicier, and C. Scott: *Micron.*, 2006, vol. 37, pp. 492–502. <https://doi.org/10.1016/j.micron.2005.10.009>.
32. B. Pereda, Z. Aretxabaleta, and B. Lopez: *J. Mater. Eng. Perform.*, 2015, vol. 24, pp. 1279–93. <https://doi.org/10.1007/s11665-015-1387-3>.
33. L. Garcia-Sesma, B. Lopez, and B. Pereda: *Metals*, 2020, vol. 10(2). <https://doi.org/10.3390/met10020165>.
34. J.O. Andersson, T. Helander, L. Höglund, P.F. Shi, and B. Sundman: *Calphad.*, 2002, vol. 26, pp. 273–312. [https://doi.org/10.1016/S0364-5916\(02\)00037-8](https://doi.org/10.1016/S0364-5916(02)00037-8).
35. L. Llanos, B. Pereda, and B. Lopez: *Metall. Mater. Trans. A.*, 2015, vol. 46A, pp. 5248–65. <https://doi.org/10.1007/s11661-015-3066-2>.

36. M. Charleux, W.J. Poole, M. Militzer, and A. Deschamps: *Metall. Mater. Trans. A.*, 2001, vol. 32A, pp. 1635–47. <https://doi.org/10.1007/s11661-001-0142-6>.
37. T. Sakuma and R.W.K. Honeycombe: *Met. Sci.*, 1984, vol. 18, pp. 449–54. <https://doi.org/10.1179/030634584790419791>.
38. P.D. Hodgson and R.K. Gibbs: *ISIJ Int.*, 1992, vol. 32, pp. 1329–38. <https://doi.org/10.2355/isijinternational.32.1329>.
39. R. Bengochea, B. Lopez, and I. Gutierrez: *Metall. Mater. Trans. A.*, 1998, vol. 29A, pp. 417–26. <https://doi.org/10.1007/s11661-998-0122-1>.
40. G. Krauss and S.W. Thompson: *ISIJ Int.*, 1995, vol. 35, pp. 937–45. <https://doi.org/10.2355/isijinternational.35.937>.
41. P. Zhang, S.X. Li, and Z.F. Zhang: *Mater. Sci. Eng. A.*, 2011, vol. 529, pp. 62–73. <https://doi.org/10.1016/j.msea.2011.08.061>.
42. A. DeArdo: *Int. Mater. Rev.*, 2003, vol. 48, pp. 371–402. <https://doi.org/10.1179/095066003225008833>.
43. A. Iza-Mendia and I. Gutierrez: *Mater. Sci. Eng. A.*, 2013, vol. 561, pp. 40–51. <https://doi.org/10.1016/j.msea.2012.10.012>.
44. L. Sanz, B. Pereda, and B. Lopez: *Mater. Sci. Eng. A.*, 2017, vol. 685, pp. 377–90. <https://doi.org/10.1016/j.msea.2017.01.014>.
45. T. Gladman, in *The Physical Metallurgy of Microalloyed Steels, Chapter: Microstructure-Property Relationships*, The Institute of Materials, London, 1997, pp. 42–45.
46. M. Calcagnotto, D. Ponge, E. Demir, and D. Raabe: *Mat. Sci. Eng. A.*, 2010, vol. 527, pp. 2738–46. <https://doi.org/10.1016/j.msea.2010.01.004>.
47. S.S. Campos, H.J. Kestenbach, and E.V. Morales: *Metall. Mater. Trans. A.*, 2001, vol. 32A, pp. 1245–8. <https://doi.org/10.1007/s11661-001-0133-7>.
48. M.E. Bush and P.M. Kelly: *Acta Metall.*, 1971, vol. 19, pp. 1363–71. [https://doi.org/10.1016/0001-6160\(71\)90074-5](https://doi.org/10.1016/0001-6160(71)90074-5).
49. D.N. Hanlon, J. Sietsma, and S. van der Zwaag: *ISIJ Int.*, 2001, vol. 41, pp. 1028–36. <https://doi.org/10.2355/isijinternational.41.1028>.
50. B. Dutta and C.M. Sellars: *Mater. Sci. Technol.*, 1987, vol. 3, pp. 197–206. <https://doi.org/10.1179/mst.1987.3.3.197>.
51. T. Gladman: *Mater. Sci. Technol.*, 1999, vol. 15, pp. 30–6. <https://doi.org/10.1179/026708399773002782>.

**Publisher's Note** Springer Nature remains neutral with regard to jurisdictional claims in published maps and institutional affiliations.